Induction Pump for High-Temperature Molten Metals Using Rotating Twisted Magnetic Field: Thrust Measurement Experiment With Solid Conductors

Tsutomu Ando, Kazuyuki Ueno, Shoji Taniguchi, and Toshiyuki Takagi, *Member, IEEE*

***Abstract*—We propose a new electromagnetic pump, applicable to high-temperature molten metal in cylindrical ducts. A rotating twisted magnetic field is generated by the stator with three pairs of helical windings. Axial thrust, as well as rotational torque, acts on the secondary conductor. It is verified that the thrust is actually obtained in experiments with a prototype stator and solid secondary conductors (bulk rotors). We discuss the slip-thrust curve for various conductivities of the secondary conductors.**

***Index Terms*—Electromagnetic pump, induction machine, linear motors, skin depth, windings.**

I. Introduction

ONE OF THE major advantages of electromagnetic force is its direct action on objects without any contact. This advantage is effectively realized in many machines. In particular, electromagnetic induction pumps and stirrers have superior endurance to mechanical pumps/stirrers and electromagnetic dc pumps/stirrers, because direct action of electromagnetic force without impellers and electrodes results in simple design with fewer damaged parts. Recently, applications of electromagnetic force have been developed in the steelmaking process, where stable performance under harsh environment is required [1]–[3].

Until now, there has been no electromagnetic pump applicable to high-temperature molten metals, for example, molten steel of over 1500 °C. At present, electromagnetic induction machines are mainly used for stirring high-temperature molten metal [4]. Conventional induction machines are not suitable for pumping molten metal against pressure gradient because counterflow occurs in certain parts of the cross section. In order to overcome this problem, a flat linear induction pump (FLIP) [5] has copper short-circuit plates that are installed in the ducts. But these plates are damaged by high temperature as well as electrodes of dc machines. An annular linear induction pump (ALIP) [5], which is an exceptional type that does not need copper short-circuit plates, has an iron core installed in the duct so that the magnetic field may traverse the flow. But the iron core loses the ferromagnetic property when temperature is higher than its Curie point. Moreover, pillars that support the iron core are seriously damaged by high temperature. As a result, the FLIP and the ALIP are not applicable to high-temperature molten metals.

In this paper, a new electromagnetic induction machine is proposed. The stator of this machine generates a rotating twisted magnetic field by a helical coil. This field gives axial thrust to a secondary conductor as well as rotational torque. This machine has both properties of the linear pump and the rotary stirrer if this machine is applied to high-temperature molten metal.

Similar helical coils are used in a helical motion induction motor (HMIM) by Rabiee and Cathey [6] and an electromagnetic stirrer by Partinen *et al.* [7]. Rabiee and Cathey developed an actuator with two degrees of freedom by coaxial connection of two HMIMs. The secondary conductor of their HMIM consists of a ferromagnetic shaft surrounded by a concentric copper sleeve. The electromagnetic force acts on only the surface of the shaft and the copper sleeve. Partinen *et al.* developed the electromagnetic stirrer for material processing. Electromagnetic force of their machine does not act on the center part of the secondary conductor owing to the four-pole magnetic field. On the other hand, electromagnetic force of the proposed pump is expected to act in good homogeneity in the cross section owing to two-pole magnetic field. Consequently, the proposed pump does not cause a counterflow. The pole number is a dominant specification for electromagnetic pumps.

This paper illustrates the principle how thrust acts on a secondary conductor in the rotating twisted magnetic field. Furthermore, it is verified that the thrust is actually obtained in a thrust measurement experiment with a prototype stator and solid secondary conductors (bulk rotors). In this experiment, secondary conductors are three types of solid cylindrical metals: copper (Cu), brass (Cu–40Zn) and stainless steel (Fe–18Cr–8Ni). Two kinds of tests, the lock test and the free-rotation test, are carried out with these secondary conductors. According to the experimental data, the slip-thrust curve of the proposed machine is compared with the slip-thrust curve of ordinary linear motors and the slip-torque curve of ordinary rotary motors.

II. Rotating Twisted Magnetic Field and Electromagnetic Force

Three pairs of helical windings, as shown in Fig. 1(b), are adopted in order to generate a rotating twisted magnetic field. It

Manuscript received April 10, 2001; revised November 13, 2001. This work was supported in part by the Matsuda Foundation's Research Grant, the Casio Science Foundation's Research Grant, and the Ministry of Education, Science, Sports and Culture, Grant-in-Aid for Scientific Research on Priority Areas 10211202.

T. Ando, K. Ueno are with Department of Aeronautics and Space Engineering, Graduate School of Engineering, Tohoku University, Sendai 980-8579, Japan (e-mail: ando@cfd.mech.tohoku.ac.jp).

S. Taniguchi is with Department of Metallurgy, Graduate School of Engineering, Tohoku University, Sendai 980-8579, Japan.

T. Takagi is with Institute of Fluid Science, Tohoku University, Sendai 980-8577, Japan.

Publisher Item Identifier S 0018-9464(02)06368-9.

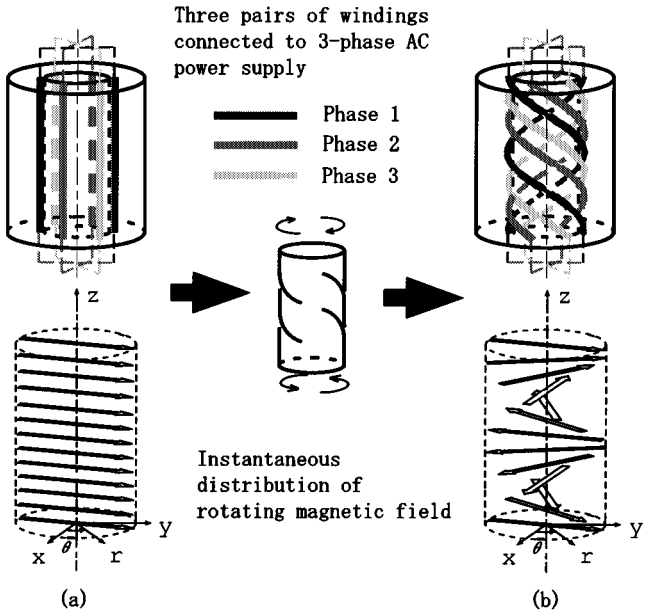

Fig. 1. Windings and magnetic field. (a) Stator of an ordinary three-phase two-pole induction motor. (b) Stator of the induction pump for high-temperature molten metals: three pairs of helical windings and rotating twisted magnetic field.

is an improved device of the stator coil of ordinary rotary induction motor, which is shown in the upper half of Fig. 1(a). The rotating magnetic field generated by the ordinary three-phase two-pole induction motor is uniform, as shown in the lower half of Fig. 1(a), and it rotates in the cross section (x–y plane) of the secondary conductor. This magnetic field is independent of the z coordinate. If this stator is twisted, windings are twisted together into helical shape, as shown in the upper half of Fig. 1(b). Since this coil has three-phase two-pole windings, the magnetic field rotates in the cross section (x–y plane) of the secondary conductor. Meanwhile, the direction of the field vector changes with z, because the windings are helical. This magnetic field rotates at a constant speed keeping the spatial distribution, as shown in Fig. 1(b).

The rotating twisted magnetic field is traveling along the z direction as well as rotating in the x–y plane. This is a necessary property for obtaining the axial thrust. We draw an analogy between the rotating twisted magnetic field and impellers of axial-flow turbo-pumps, in which straight motion is caused by rotation of twisted matter.

The phase difference among three-phase current of ordinary linear induction machines deviates from $2\pi/3$ owing to the end effect. On the other hand, the phase difference of three-phase current shown in Fig. 1(b) is $2\pi/3$ because the three pairs of windings are equivalent to one another. Therefore, the proposed machine does not have an energy loss by the phase shift, and has no need of compensation windings and compensation circuits.

A secondary conductor is installed in the rotating twisted magnetic field, as shown in Fig. 2(a). This study is based on the following hypothesis. The rotating twisted magnetic field generates the induced current in the secondary conductor, as shown in Fig. 2(b). This current is short-circuited upstream and downstream outside of the stator length. When the secondary conductor rotates near the synchronous speed, the phase difference between the primary coil current and the secondary current is $\pi/2$ similar to the ordinary induction motor. Now we pay attention to a G–G cross section of the secondary conductor, and set the y axis along the instantaneous magnetic field in a certain moment. Since the z component of the current density j_z is antisymmetric with respect to the center of the cross section (an odd function of y), the transverse component of the Lorentz force represents a pair of forces, as shown in Fig. 2(c). In other words, rotational torque is obtained. Next, we pay attention to an H–H longitudinal section of the secondary conductor containing the magnetic field vector. The x component of the current density j_x is symmetric with respect to the z axis (an even function of y). Therefore, the axial component of the Lorentz force is unidirectional all over the secondary conductor, as shown in Fig. 2(d). Consequently, the rotating twisted magnetic field gives axial thrust to the secondary conductor as well as rotational torque.

On the above hypothesis, the distribution of the magnetic flux density in the cross section is out of consideration. But nonuniformity of the magnetic field is not negligible if the twist angle of the helical windings is large. Quantitative discussion about the distribution of the magnetic field is given in the Appendix.

III. Experimental Apparatus

A. Stator

A prototype stator with three pairs of helical windings has been fabricated in order to verify the hypothesis of Section II, meaning that axial thrust by the rotating twisted magnetic field can be obtained. The photograph and main specification of this stator are shown in Fig. 3 and Table I, respectively. Sheets of silicon steel, as shown in Fig. 4, are piled up while sliding in a circumferential direction. They form a yoke with twisted slots. The twist angle is 45° on the inner surface. Windings are installed in the slots of this yoke.

B. Magnetic Flux Density

The distribution of the magnetic flux density in the stator was measured with a Hall-probe when the bore of the stator was empty. Root-mean-square (rms) values and instantaneous values of the magnetic flux density were measured with the Hall-probe.

At first, the Lissajous figure was displayed on an oscilloscope by instantaneous signal of the magnetic flux density and the primary current. Observation of the Lissajous figure for various locations and various angles of the probe confirmed the generation of the rotating twisted magnetic field.

Next, the magnetic flux density in a cross section was measured with the probe fixed on an xyz-stage. Table II shows averages of rms values of measurement and predictions of the magnetic flux density in the central cross section $z = 0$ mm when $\bar{\mathcal{I}} = 10$ A, $\mathcal{N} = 50$. Predicted values are given by (21) in the Appendix. The averaged measurement values at the same radius agree with the predicted values within an error of 7% even though the predicted value is an approximation by an ideal current sheet. Therefore, it was confirmed that this stator satisfactorily shows the fundamental performance of the proposed induction machine.

However, the distribution of the measured magnetic flux density has remarkable spatial higher harmonics. Unfortunately, it

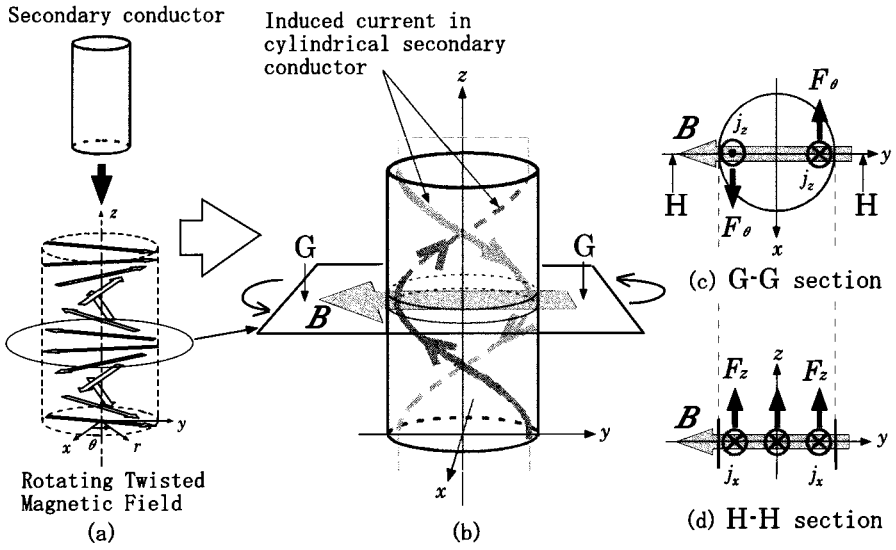

Fig. 2. Lorentz force by the rotating twisted magnetic field. (a) Secondary conductor installed in the rotating twisted magnetic field. (b) Induced current in the secondary conductor. (c) Torque in G–G cross section. (d) Thrust in H–H longitudinal section.

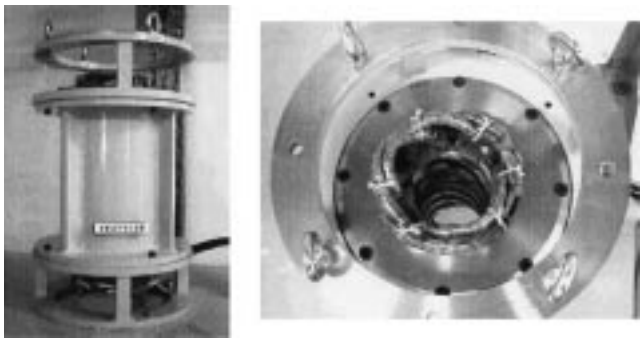

Fig. 3. Prototype of the stator.

TABLE I
SPECIFICATION OF THE STATOR

Inner diameter	ϕ 80mm
Outer diameter	ϕ 180mm
Length of the yoke	252mm
Twist angle of the coil	45 degrees
Number of coil windings ($\mathcal{N}$)	50 turn
Number of poles	2
Number of phases	3

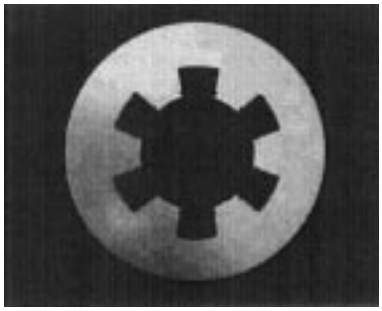

Fig. 4. Silicon steel plate with six slots.

is far beyond expectation on the design. Fig. 5 shows an example. Measured data of rms values $\bar{B}_\theta$ are plotted versus the z coordinate. The magnetic flux density $\bar{B}_\theta$ near the inner wall of

TABLE II
AVERAGE OF RMS VALUES OF MAGNETIC FLUX DENSITY IN THE CENTRAL CROSS SECTION $z = 0$ mm WHEN $\bar{I} = 10$ A, $\mathcal{N} = 50$

	$r = 0$[mm]	$r = 35$[mm]	
	$\bar{B}_x = \bar{B}_y$ [mT]	$\bar{B}_r$ [mT]	$\bar{B}_\theta$ [mT]
Measurement	14.8	17.1	15.8
Prediction†	13.9	18.1	15.3

†Predicted values are given by (21).

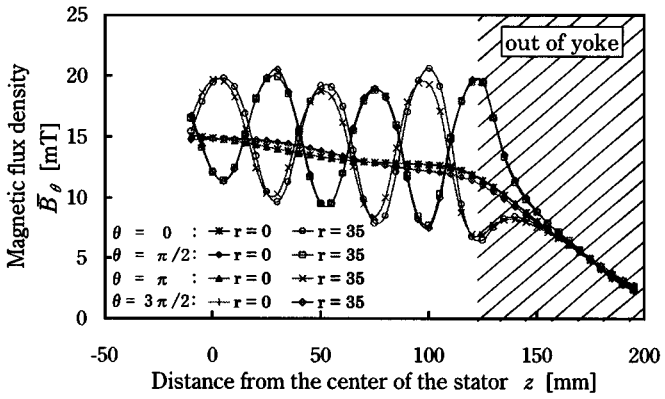

Fig. 5. Axial distribution of rms value $\bar{B}_\theta$ of magnetic flux density when $\bar{I} = 10$ A, $\mathcal{N} = 50$.

the stator has swings in response to the teeth and the slots of the stator, though $\bar{B}_\theta$ in the center $r = 0$ mm smoothly decreases toward the top of the coil $z = 126$ mm. Since the same swing with the θ coordinate was observed, the values in Table II are averaged in the points corresponding to the teeth and the slots of the stator. Considering instantaneous distribution, we can interpret these swings as spatial higher harmonics of the rotating twisted magnetic field.

C. Thrust Measurement System

Thrust acting on cylindrical solid conductors is measured. In this experiment, three types of conductor materials were

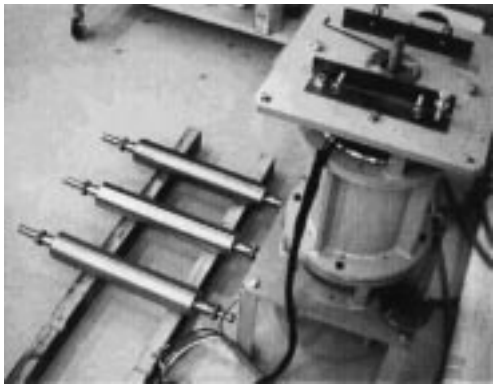

Fig. 6. Cylindrical secondary conductors of solid metals.

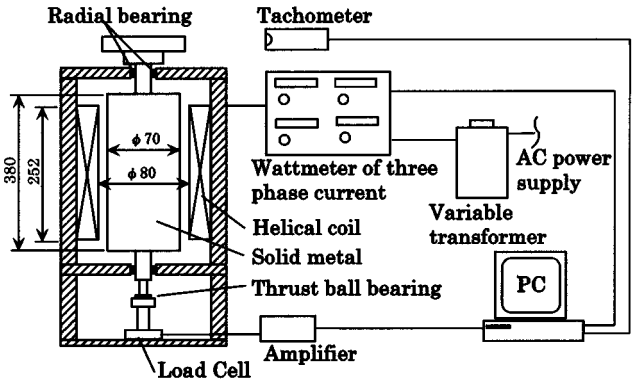

Fig. 7. Configuration of the thrust measurement system.

TABLE III
CONDUCTIVITY OF MATERIALS OF THE SECONDARY CONDUCTORS AT 293 K

Nomenclature of Materials		Conductivity σ [Sm^{-1}]
Copper	Cu	5.8×10^7
Brass	Cu-40Zn	1.5×10^7
Stainless Steel	Fe-18Cr-8Ni	0.2×10^7

used: copper (Cu), brass (Cu–40Zn), and stainless steel (Fe–18Cr–8Ni). An effective part of solid conductors is 70 mm in diameter and 380 mm in length, as shown in Fig. 6. The conductivities of these secondary conductors are shown in Table III.

The thrust measurement system is shown in Fig. 7. Axial thrust is measured with a load cell placed under the secondary conductor. Since the secondary conductor is supported by two radial roller bearings at the upper and lower frame and by a thrust ball bearing at the bottom, thrust in the axial direction is certainly received by the load cell. Rotational speed is measured with an optical tachometer. The outputs of the load cell, the tachometer and the wattmeter are sampled at every 0.25 s and recorded on a personal computer.

IV. EXPERIMENTS AND RESULTS

Table IV shows two kinds of the experimental conditions: the lock test and the free-rotation test. In the lock test, the secondary conductor was locked by a wire hanged on a bolt on the frame. This wire was horizontally hanged so as not to influence axial thrust. On the other hand, the free-rotation test was carried out without the wire.

A. Lock Test

The result of the lock test is shown in Fig. 8. This result verifies that the thrust in the axial direction acts on the secondary conductor in the rotating twisted magnetic field.

The thrust is proportional to the square of the primary current $\bar{\mathcal{I}}$. Sequences of these data give agreement with quadratic functions. The coefficients of the square of primary current $\bar{\mathcal{I}}$ are $(3.5 \pm 0.1) \times 10^{-2}$ N/A^2 for the brass cylinder, $(1.9 \pm 0.1) \times 10^{-2}$ N/A^2 for the copper cylinder, and $(1.0 \pm 0.1) \times 10^{-2}$ N/A^2 for the stainless steel cylinder, respectively. The error span of the coefficients of the quadratic curve increases with measurement time, because it is caused by temperature increase of the secondary conductor by Joule heating.

The thrust on the brass cylinder is larger than that on the copper cylinder though the conductivity of the brass is smaller than that of the copper (see Table III). This phenomenon will be discussed in Section V in detail.

B. Free-Rotation Test

The result of the free-rotation test is shown in Fig. 9. The horizontal axis is the rotational speed measured by the tachometer under acceleration of rotation. The thrust measured at a certain rotational speed on the rotational acceleration are equivalent to that on steady rotation at the same speed, because the time in which the secondary conductor is accelerated is much longer than the period 1/50 s of the rotating magnetic field. For example, the thrust at 0 rpm of the free-rotation test agrees with the result of the lock test.

Experiments were carried out several times while changing the input voltage, for example, 20, 40, and 60 V. Results for various conditions are plotted in Fig. 9. The vertical axis is the thrust divided by the square of the primary current $\bar{\mathcal{I}}$ at the corresponding rotational speed. The solid curves in the figure are the predicted functions, which will be explained in Section V. The curvilinear sequences of plotted data show that the thrust is well normalized by the square of the primary current $\bar{\mathcal{I}}$.

With respect to the brass and the stainless steel cylinders, the maximum thrust in the measured range is obtained at the starting 0 rpm, and the thrust monotonously decreases with rotational speed. This curve is similar to the slip-thrust curve of ordinary low-speed linear induction motors used for system control [8].

On the other hand, the maximum thrust of the copper cylinder is obtained at about 2300 rpm. This curve is similar to the slip-thrust curve of ordinary high-speed linear induction motors [8] and the slip-torque curve of ordinary rotary induction motors [9].

Theory and experiments of linear induction motors and rotary induction motors show that the speed of the maximum thrust (or the maximum torque) decreases as the conductivity of the secondary conductor decreases [10], [11]. These analogies suggest that the induction machines using the rotating twisted magnetic field are in the same framework with ordinary linear induction motors and ordinary rotary induction motors with respect to the slip-thrust (or slip-torque) curve.

TABLE IV
CONDITIONS OF EXPERIMENT

	Rotation	Frequency f[Hz]	Voltage V[V]	Measurement range
Lock Test	Lock	50	Manual increase	$0 \sim 30$[A]
Free-Rotation Test	Free acceleration	50	Fixed	Up to terminal rotation

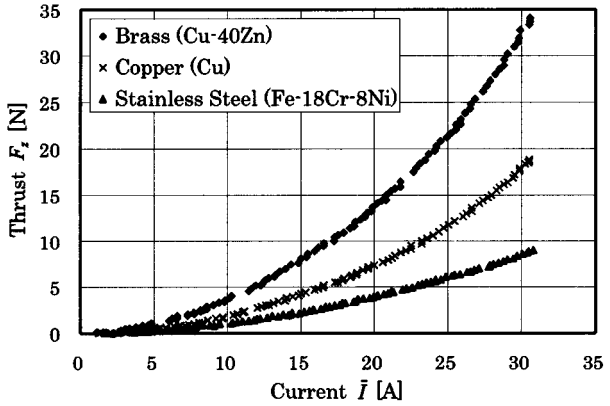

Fig. 8. Thrust on the lock tests.

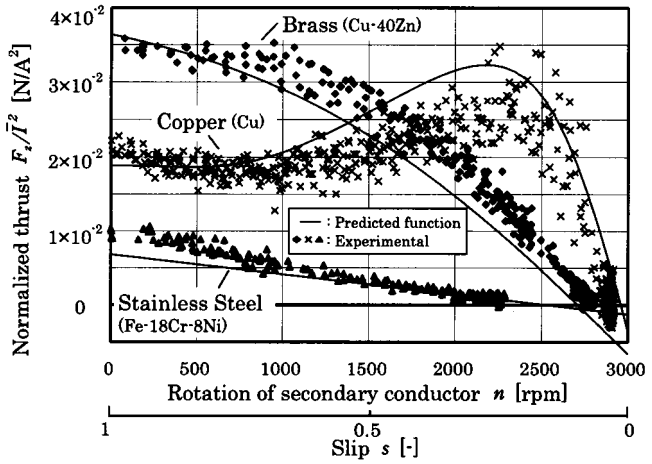

Fig. 9. Experimental results and a predicted function of the thrust on the free-rotation tests.

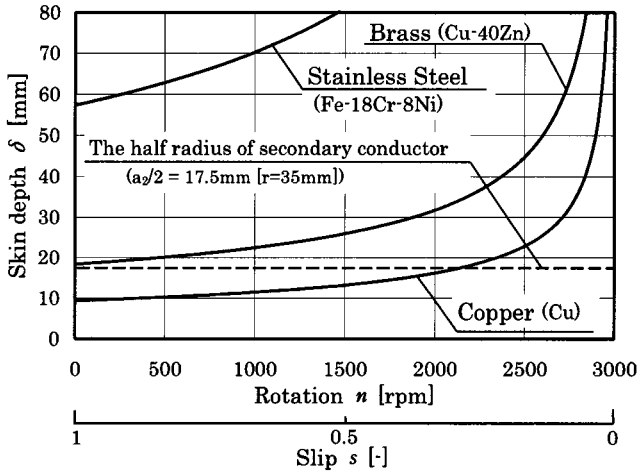

Fig. 10. Relationship between the slip and the skin depth.

TABLE V
SLOPE OF THE SLIP-THRUST CURVE AROUND THE SYNCHRONOUS CONDITION

Material	$\bar{I}^{-2}(\frac{dF_z}{ds})_{s=0}$ [NA^{-2}]	$\sigma^{-1}\bar{I}^{-2}(\frac{dF_z}{ds})_{s=0}$ [NΩmA^{-2}]
Copper	0.3	0.5×10^{-8}
Brass	0.08	0.5×10^{-8}
Stainless Steel	0.01	0.5×10^{-8}

V. DISCUSSION

A. Condition for the Maximum Thrust

In the case of the copper cylinder, the slip-thrust curve does not decrease monotonously. The similar characteristic curve of rotary squirrel-cage motors can be explained as a result of phase shift of the secondary current [12]. When a solid secondary conductor is used, we obtain simultaneous occurrence of the phase shift and the skin effect of the secondary current. Therefore, the following discussion concentrates on the skin depth.

The skin depth δ of a rotational secondary conductor is given by

$$\delta = \sqrt{\frac{1}{\mu\sigma\pi f s}} \tag{1}$$

where σ denotes the conductivity of the secondary conductor and μ denotes the magnetic permeability of the secondary conductor [8]. Slip s is a dimensionless parameter that explains the relative motion between the magnetic field and the secondary conductor. It is defined by

$$s = \frac{3000 - n}{3000} \tag{2}$$

where n denotes rotations per minute of the secondary conductor. Fig. 10 shows the skin depth of each secondary conductor given by (1). The magnetic permeability of secondary conductor is the space permeability μ_0. A broken line on this figure gives a half of radius of the secondary conductor a_2. Intersection points of the broken line and curves of the skin depth are $s \simeq 0.25$ for the copper cylinder and $s \simeq 1$ for the brass cylinder. These values nearly equal the slip of the local maximum thrust. (Here, it is interpreted that the slip-thrust curve of the brass cylinder has a local maximum at the edge $s = 1$ of the measurement range and the curve of the stainless steel cylinder does not have the local maximum in the measurement range.) This fact suggests that the maximum thrust is obtained when the skin depth is nearly equal to a half radius of the secondary conductor.

When the slip is greater than the local maximum point, the skin effect prevents the magnetic field from penetrating to the center part of the secondary conductor. If the secondary conductor is replaced by molten metal, operation in such conditions is not effective as a pump because of counterflow at the center part.

B. Thrust Around the Synchronous Condition

Theory of ordinary linear induction motors and rotary induction motors shows that the slope of the slip-thrust curve (or the slip-torque curve) around the synchronous condition $s = 0$ is proportional to the conductivity of secondary conductor [10]. Table V shows the slope $(d\mathcal{F}_z/ds)_{s=0}$ around the synchronous condition of each secondary conductor obtained from the free-rotation test (see Fig. 9). This result shows that not only ordinary induction motors, but also the induction machine using the rotating twisted magnetic field has the following relationship:

$$\left.\frac{d\mathcal{F}_z}{ds}\right|_{s=0} \propto \mu_0 \bar{\mathcal{I}}^2 \mathcal{N}^2 \sigma. \tag{3}$$

C. Predicted Function of the Slip-Thrust Curve

There are several common characteristics among the slip-thrust curve obtained from this experiment, the slip-thrust curve of ordinary linear induction motors, and the slip-torque curve of ordinary rotary induction motors. Therefore, it is supposed that the slip-thrust curve of the fundamental harmonic is expressed in the following function according to the theory of ordinary linear induction motors [13]:

$$\mathcal{F}_{z0} = \mu_0 \bar{\mathcal{I}}^2 \mathcal{N}^2 \frac{2A_f c R_\omega s}{1 + (cR_\omega s)^2} \tag{4}$$

where R_ω denotes the shielding parameter

$$R_\omega = 2\pi\sigma\mu_0 f a^2. \tag{5}$$

The constants A_f and c in (4) are decided by comparing the curve with experimental data. In (5), a is a radius of the stator. The function (4) has a local maximum value $\mathcal{F}_{z0} = \mu_0 \bar{\mathcal{I}}^2 \mathcal{N}^2 A_f$ at $s = (cR_\omega)^{-1}$.

As mentioned in Section III-B, six teeth and slots of the yoke cause fifth and seventh spatial higher harmonics. These synchronous speeds are -600 rpm $(s = 6/5)$ and 428 rpm $(s = 6/7)$, respectively. Taking account of fifth and seventh spatial higher harmonics, we obtain the slip-thrust curve of superposition [12] as follows:

$$\mathcal{F}_z = \mu_0 \bar{\mathcal{I}}^2 \mathcal{N}^2 \left\{ \frac{2A_f c R_\omega s}{1 + (cR_\omega s)^2} + \frac{2A_h c R_\omega \left(s - \frac{6}{5}\right)}{1 + \left[cR_\omega \left(s - \frac{6}{5}\right)\right]^2} + \frac{2A_h c R_\omega \left(s - \frac{6}{7}\right)}{1 + \left[cR_\omega \left(s - \frac{6}{7}\right)\right]^2} \right\} \tag{6}$$

where A_h is a constant decided by comparing the curve with experimental data.

Substituting $A_f = 11.7$, $A_h = 1.06$, and $c = 0.096$ for (6), we drew three curves in Fig. 9 for each conductivity of the three secondary conductors. Here, the constant c is given by the local maximum condition $s = (cR_\omega)^{-1}$ of the function and $\delta = a_2/2$ of the experimental data. Meanwhile, the constants A_f and A_h are decided by comparing the curve with experimental data. The predicted function (6) gives a fairly good approximation of the experimental data. This function with the above constants can predict the slip-thrust curve for arbitrary material of the secondary conductor.

The constant A_h is not negligibly small for the prototype stator. As a result, the rotational speed for $\mathcal{F}_z = 0$ has a certain difference from the synchronous speed 3000 rpm of the fundamental harmonics. This phenomenon is one of the effects of the spatial higher harmonics.

VI. Conclusion

A new electromagnetic induction pump that gives axial thrust to high-temperature molten metal in cylindrical ducts is proposed. The stator with three pairs of helical windings generates a rotating twisted magnetic field. The principle how axial thrust acts on the secondary conductor in the rotating twisted magnetic field is illustrated in this paper.

Thrust measurement experiments are carried out with a prototype stator and solid secondary conductors. The following results are obtained through the experiments.

1) The rotating twisted magnetic field is generated by the stator with three pairs of helical windings.
2) The average value of magnetic flux density agrees with the predicted value within an error of 7% though the magnetic flux density near the inner wall of the stator, which includes undesirable higher harmonics due to the teeth and the slots of the stator.
3) The axial thrust is obtained from the rotating twisted magnetic field and it is proportional to the square of the primary current.
4) The rotational speed for the local maximum thrust depends on the conductivity of secondary conductor. The experimental data suggest that the maximum thrust is obtained when the skin depth is nearly equal to a half radius of the secondary conductor.
5) A function for the prediction of the slip-thrust curve is proposed, and it is in fairly good agreement with the experimental data.

Appendix
Rotating Twisted Magnetic Field Without the Secondary Conductor

Three pairs of helical windings are installed at $\theta + kz = m\pi/3$ $(m = 0, 1, 2, 3, 4, 5)$ and the number of each windings is $\mathcal{N}$, where k denotes a wave number in the z direction. The angle between the z axis and helical windings is $\tan^{-1}(kr)$. The current of the mth-phase winding is

$$\mathcal{I}_m = \sqrt{2}\bar{\mathcal{I}} \cos\left(2\pi f t - \frac{m\pi}{3}\right) \tag{7}$$

where $\bar{\mathcal{I}}$ A denotes the rms of the current from the electric power supply, f Hz denotes the frequency. Since this is a kind of the three-phase two-pole machine, both the electrical and geometrical angles of the windings are $m\pi/3$.

To simplify the problem, the primary current is replaced with a cylindrical current sheet as shown in Fig. 11. The radius of the current sheet is denoted by a. This radius corresponds to the distance from the center to the inner face of the teeth of the actual stator. The sheet current of the current sheet is denoted by (i_θ, i_z) A/m. It is required that a sheet current is a continuous function of θ, z and the following relation is satisfied:

$$\int_{((1/3)m\pi - (1/6)\pi - \theta)k^{-1}}^{((1/3)m\pi + (1/6)\pi - \theta)k^{-1}} i_\theta \, dz = \mathcal{I}_m \mathcal{N} \tag{8}$$

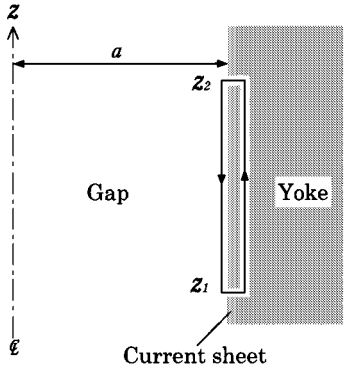

Fig. 11. Current sheet.

$$\int_{(1/3)m\pi-(1/6)\pi-kz}^{(1/3)m\pi+(1/6)\pi-kz} i_z a\, d\theta = -\mathcal{I}_m \mathcal{N}. \tag{9}$$

A sheet current

$$i_\theta = \sqrt{2}\bar{\mathcal{I}}\mathcal{N}k\cos(2\pi ft-\theta-kz) \tag{10}$$

$$i_z = -\sqrt{2}\bar{\mathcal{I}}\mathcal{N}a^{-1}\cos(2\pi ft-\theta-kz) \tag{11}$$

satisfies the above requirements.

The sheet current always satisfies the relation $i_\theta/i_z = -ka$. On the other hand, a small line element on the curve $\theta + kz = \text{constant}$ satisfies the relation $ad\theta/dz = -ka$. Therefore, the following relation is obtained:

$$\frac{i_\theta}{ad\theta} = \frac{i_z}{dz}. \tag{12}$$

Consequently, the sheet current (10) and (11) is parallel to the helical lines $\theta + kz = \text{constant}$.

The Ampère's law in the integral representation is applied to a closed loop across the current sheet as shown in Fig. 11

$$\int_{z_1}^{z_2}\left[\frac{B_z}{\mu}\right]_{\text{yoke}} dz + \int_{z_2}^{z_1}\left[\frac{B_z}{\mu_0}\right]_{\text{gap}} dz = -\int_{z_1}^{z_2} i_\theta\, dz \tag{13}$$

$$\int_{\theta_1}^{\theta_2}\left[\frac{B_\theta}{\mu}\right]_{\text{yoke}} a\, d\theta + \int_{\theta_2}^{\theta_1}\left[\frac{B_\theta}{\mu_0}\right]_{\text{gap}} a\, d\theta = \int_{\theta_1}^{\theta_2} i_z a\, d\theta. \tag{14}$$

Since the integral range is arbitrarily selected, the following equations are obtained:

$$\left[\frac{B_z}{\mu}\right]_{\text{yoke}} - \left[\frac{B_z}{\mu_0}\right]_{\text{gap}} = -i_\theta \tag{15}$$

$$\left[\frac{B_\theta}{\mu}\right]_{\text{yoke}} - \left[\frac{B_\theta}{\mu_0}\right]_{\text{gap}} = i_z. \tag{16}$$

Assuming an ideal yoke $[\mu]_{\text{yoke}}/\mu_0 \gg 1$, we obtain

$$[B_z]_{\text{gap}} = \mu_0 i_\theta \tag{17}$$

$$[B_\theta]_{\text{gap}} = -\mu_0 i_z. \tag{18}$$

Substituting (10) and (11) for (17) and (18), we obtain the tangential component of the magnetic flux density at the outer boundary of the air gap

$$[B_\theta]_{\text{gap}} = \sqrt{2}\mu_0\bar{\mathcal{I}}\mathcal{N}a^{-1}\cos(2\pi ft-\theta-kz) \text{ at } r=a \tag{19}$$

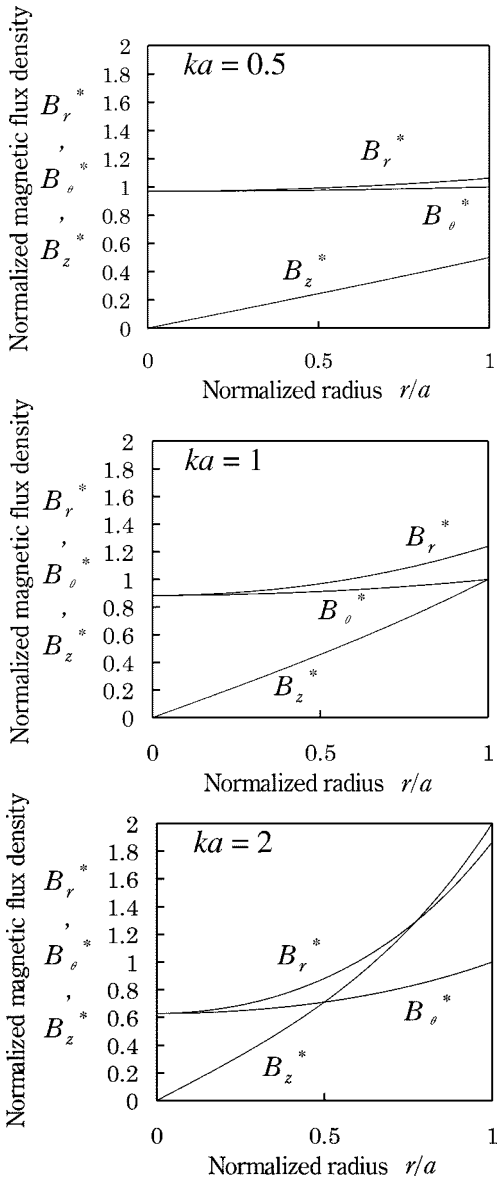

Fig. 12. Radial distribution of the amplitude of the magnetic flux density for various twist angles.

$$[B_z]_{\text{gap}} = \sqrt{2}\mu_0\bar{\mathcal{I}}\mathcal{N}k\cos(2\pi ft-\theta-kz) \text{ at } r=a. \tag{20}$$

If a secondary conductor is not installed in the stator, the distribution of the magnetic flux density in the stator is given by a solution of Laplace's equation. The solution satisfying the boundary conditions (19) and (20) are

$$\begin{aligned} B_r &= -\frac{\sqrt{2}\mu_0\bar{\mathcal{I}}\mathcal{N}}{a}\frac{I_0(kr)-(kr)^{-1}I_1(kr)}{(ka)^{-1}I_1(ka)} \\ &\quad\times\sin(2\pi ft-\theta-kz) \\ B_\theta &= \frac{\sqrt{2}\mu_0\bar{\mathcal{I}}\mathcal{N}}{a}\frac{aI_1(kr)}{rI_1(ka)}\cos(2\pi ft-\theta-kz) \\ B_z &= \frac{\sqrt{2}\mu_0\bar{\mathcal{I}}\mathcal{N}}{a}\frac{kaI_1(kr)}{I_1(ka)}\cos(2\pi ft-\theta-kz) \end{aligned} \tag{21}$$

where I_0 and I_1 denote the modified Bessel functions of the first order. The magnitude of the magnetic flux density is pro-

portional to $\bar{\mathcal{I}}\mathcal{N}$. The angular velocity and the traveling velocity in the z direction are $2\pi f$ and $2\pi f/k$, respectively.

When a secondary conductor is installed in the stator, (21) becomes the first approximation. It is useful for a small slip condition, because the induced current in the secondary conductor is small when the speed of a secondary conductor is close to the synchronous speed. In such a condition, the magnetic flux density in the cross section is well uniform when $ka \ll 1$. But in this case, the thrust is not enough because the twist is very small. When $ka \sim 1$, uniformity of B_r and B_θ is slightly bad, because B_z is not negligible. When $ka \gg 1$, the magnetic field is reduced around the center part, and the advantages of the two-pole machine are lost. Distributions of B_r, B_θ, and B_z in the case of $ka = 0.5, 1$, and 2 are shown in Fig. 12. The variable ${B_r}^*$, ${B_\theta}^*$, and ${B_z}^*$ are the dimensionless amplitude normalized by $\sqrt{2}\mu_0\bar{\mathcal{I}}\mathcal{N}a^{-1}$. In order to obtain strong and uniform thrust in the cross section, we must adopt an appropriate twist angle about $ka \sim 1$ (45°).

ACKNOWLEDGMENT

The authors would like to thank Prof. T. Kenjo of Polytechnic University of Japan for helpful discussions on the electrical characteristic of induction machines, and T. Sato of Institute of Fluid Science, Tohoku University, for help of detail design of experimental equipments.

REFERENCES

[1] M. Garnier, "Technological and economical challenges facing EPM in the next century," in *Proc. Int. Symp. Electromagnetic Processing of Materials*, Nagoya, Japan, Apr. 3–6, 2000, pp. 3–8.

[2] T. Fujii, "State of art electromagnetic processing in Japanese iron and steel industry," in *Proc. Int. Symp. Electromagnetic Processing of Materials*, Nagoya, Japan, Apr. 3–6, 2000, pp. 14–19.

[3] E. Takeuchi and K. Miyazawa, "Electromagnetic casting technology of steel," in *Proc. Int. Symp. Electromagnetic Processing of Materials*, Nagoya, Japan, Apr. 3–6, 2000, pp. 20–27.

[4] D. Bialod, Ed., *Electromagnetic Induction and Electric Conduction in Industry*: Centre Français de l'Électricité, 1997, pp. 359–362.

[5] L. R. Blake, "Conduction and induction pumps for liquid metals," in *Proc. Inst. Elect. Eng.*, 1956, pp. 49–63.

[6] M. Rabiee and J. J. Cathey, "Verification of a field theory analysis applied to a helical motion induction motor," *IEEE Trans. Magn.*, vol. 24, pp. 2125–2132, July 1988.

[7] J. Partinen, N. Saluja, J. Szekely, and J. Kirtley Jr., "Experimental and computational investigation of rotary electromagnetic stirring in a woods metal system," *ISIJ Int.*, vol. 34, pp. 707–714, 1994.

[8] S. Yamamura, *Theory of Linear Induction Motors*. Tokyo, Japan: Univ. Tokyo Press, 1978, pp. 42–91.

[9] P. L. Alger, *The Nature of Polyphase Induction Machines*. New York: Wiley, 1951, pp. 96–99.

[10] E. R. Laithwaite, *Propulsion Without Wheels*. New York: Hart, 1968, pp. 81–117.

[11] T. Wildi, *Electrical Machines, Drives, and Power Systems*. Englewood Cliffs, NJ: Prentice-Hall, 1997, pp. 276–278.

[12] P. L. Cochran, *Polyphase Induction Motors*. New York: Marcel Dekker, 1989, pp. 82–458.

[13] B. T. Ooi and D. C. White, "Traction and normal forces in the linear induction motor," *IEEE Trans. Power App. Syst.*, vol. PAS-89, no. 4, pp. 638–645, 1970.

Tsutomu Ando was born in Saitama, Japan, on July 20, 1967. He received the B.S. degree in mechanical engineering from Chiba University in 1991.

From 1991 to 1996, he was a mechanical engineer of the space experiment system development department, Ishikawajima-Harima Heavy Industries Co., Ltd. Since 1999, he has been a graduate student at School of Engineering, Tohoku University, conducting research on MHD pumps.

Kazuyuki Ueno received the B.S., M.S., and Ph.D. degrees in aeronautical engineering from Kyoto University, Japan, in 1988, 1990, and 1993, respectively.

He has been an Associate Professor at the Graduate School of Engineering, Tohoku University, Sendai, Japan, since 2001. He was a research associate from 1993 to 1998 and a lecturer from 1998 to 2001 at the Institute of Fluid Science, Tohoku University. His current research interests include magnetohydrodynamics, electromagnetic processing of materials, and multiphase flow.

Shoji Taniguchi received the B.Eng., M.Eng., and D.Eng. degrees from Tohoku University, Japan, in 1972, 1974, and 1977, respectively.

He was a research associate from 1977 to 1984, and an Associate Professor from 1984 to 1996 at the Faculty of Engineering, Tohoku University, Sendai, Japan. He has been a Professor at the Graduate School of Engineering, Tohoku University, since 1996. His major field is metallurgical engineering, and current research interests include chemical kinetics of refining reaction of metals, fluid flow and mass transfer in gas-injected metallurgical vessel, agglomeration of inclusion particles in liquid metal, and application of electromagnetic force to metallurgy.

Toshiyuki Takagi (M'88) received the B.S., M.S., and Ph.D. degrees in nuclear engineering from the University of Tokyo, Japan, in 1977, 1979, and 1982, respectively.

He has been a Professor at the Institute of Fluid Science, Tohoku University, Sendai, Japan, since 1998. He was a researcher at the Energy Research Laboratory of Hitachi Ltd. from 1982 to 1987. He was an Associate Professor at the Nuclear Engineering Research Laboratory of the University of Tokyo from 1987 to 1989, and an Associate Professor at the Institute of Fluid Science, Tohoku University, from 1989 to 1998. His current research interests include adaptive structural systems using shape memory alloys, electromagneto-mechanical behavior of functional materials, and nondestructive evaluation of materials using electromagnetic phenomena.